

On the consistency of pseudo-potential lattice Boltzmann methods

Luiz Eduardo Czelusniak,¹ Tim Niklas Bingert,² Mathias J. Krause,^{1,2} and Stephan Simonis¹

¹*Lattice Boltzmann Research Group (LBRG), Institute for Applied and Numerical Mathematics (IANM), Karlsruhe Institute of Technology (KIT), Karlsruhe, Baden Württemberg, D-76131, Germany*

²*Lattice Boltzmann Research Group (LBRG), Institute of Mechanical Process Engineering (MVM), Karlsruhe Institute of Technology (KIT), Karlsruhe, Baden Württemberg, D-76131, Germany*

(*Electronic mail: luiz.czelusniak@partner.kit.edu)

(Dated: 22 April 2025)

We derive the partial differential equation (PDE) to which the pseudo-potential lattice Boltzmann method (P-LBM) converges under diffusive scaling, providing a rigorous basis for its consistency analysis. By establishing a direct link between the method’s parameters and physical properties—such as phase densities, interface thickness, and surface tension—we develop a framework that enables users to specify fluid properties directly in SI units, eliminating the need for empirical parameter tuning. This allows the simulation of problems with predefined physical properties, ensuring a direct and physically meaningful parametrization. The proposed approach is implemented in OpenLB, featuring a dedicated unit converter for multiphase problems. To validate the method, we perform benchmark tests—including planar interface, static droplet, Galilean invariance, and two-phase flow between parallel plates—using R134a as the working fluid, with all properties specified in physical units. The results demonstrate that the method achieves second-order convergence to the identified PDE, confirming its numerical consistency. These findings highlight the robustness and practicality of the P-LBM, paving the way for accurate and user-friendly simulations of complex multiphase systems with well-defined physical properties.

I. INTRODUCTION

The lattice Boltzmann method (LBM) has emerged as a promising tool for simulating multiphase systems^{1–5}, primarily due to its high computational efficiency, particularly in parallel simulations using multicore CPUs^{6–8} and GPUs^{9,10}. Several multiphase approaches exist within the LBM framework, including the pseudo-potential^{11,12}, free-energy^{13,14}, phase-field^{15–17}, and color-gradient methods^{18,19}. Among these, the pseudo-potential method (P-LBM) is particularly useful for high-performance simulations^{20,21} due to its simplicity and efficiency²². The interface naturally emerges from the interparticle forces acting on the fluid²³, eliminating the need for interface capturing or tracking methods.

However, many simulations using the P-LBM are conducted using lattice units without establishing a clear correspondence between the simulation and a real physical condition²⁴. Baakeem, Bawazeer, and Mohamad²⁵ argue that the conversion or mapping of parameters between the macroscopic (or physical) scale and the mesoscopic (or lattice) scale is not a straightforward procedure for the P-LBM. Therefore, some authors have focused on the dimensional analysis of this method^{24–28}. As a result, different strategies for mapping parameters between the macroscopic and mesoscopic scales were proposed.

Despite the progress, some points still make P-LBM challenging to apply to real physical problems. First, the method relies on specifying the properties of the equation of state (EOS), whereas the phase-field method allows for the direct imposition of surface tension and interface thickness, making it more practical to use. Another difficulty mentioned by Czelusniak *et al.*²² is that the method’s parameters, necessary to impose the desired surface tension and ensure thermodynamic consistency, must be found empirically through prior simulations such as the Young–Laplace test.

To address these issues, we revisited the topic of P-LBM consistency. Through our investigation, we derived the form of the macroscopic equation to which the P-LBM converges under diffusive scaling. This understanding allowed us to directly relate the fluid’s physical properties—such as phase densities, interface thickness, and surface tension—to the P-LBM parameters. Consequently, one of the method’s major limitations was addressed: Users no longer need to fine-tune specific parameters, but can instead define desired fluid properties directly, greatly simplifying its application.

To implement and validate these developments, we utilized OpenLB²⁹ based on version 1.7³⁰. This software is a powerful tool for parallel lattice Boltzmann simulations that is employed for example in sub-grid particulate flows³¹, fully resolved particle flows^{8,32}, turbulence simulations^{33,34}, optimization^{35,36}, sub-grid multiphase flows³⁷ and fully resolved multiphase flows³⁸. OpenLB employs unit converters, enabling users to specify physical variables directly in physical units that are then transformed into lattice units by the converter. We extended this framework by developing a dedicated converter for multiphase problems. This enhancement allows users to define fluid properties not only directly but also in physical units, making the method significantly more user-friendly and versatile.

To validate our approach, we selected four benchmarks with analytical solutions for diffuse interface problems: planar interface, static droplet, Galilean invariance, and two-phase flow between parallel plates. All tests are performed in SI units using R134a as a working fluid. Each problem was solved using meshes with varying resolutions, and we demonstrated that the method achieves second-order convergence in all cases, confirming its consistency.

The remainder of this paper is organized as follows. In Section II, we introduce the theoretical foundations of the pseudo-potential lattice Boltzmann method (P-LBM). Section III fo-

cuses on the derivation of the partial differential equation (PDE) approximated by the P-LBM under diffusive scaling. In Section IV, we present the methodology for directly relating the method parameters to physical properties. Section V describes the implementation of the proposed framework in OpenLB, including the development of a dedicated unit converter for multiphase problems. Section VI presents the results of the benchmark tests, validating the consistency of the method. Finally, Section VII concludes the paper with a summary of the main findings.

II. PSEUDO-POTENTIAL LBM

In this work, we apply the lattice Boltzmann equation (LBE) with the single-relaxation-time (SRT or BGK) collision operator³⁹. To establish the dimensions of each variable, we define the fundamental dimensions of mass (M), length (L), and time (T). We denote the dimension of a variable ϕ as $[\phi]$. The LBE is expressed as:

$$f_i(t + \Delta t, \mathbf{x} + \mathbf{c}_i \Delta t) - f_i(t, \mathbf{x}) = -\frac{\Delta t}{\tau} (f_i - f_i^{eq}) + \Delta t F_i', \quad (1)$$

where f_i ($[f_i] = ML^{-3}$) are the particle distribution functions associated with particle velocities \mathbf{c}_i , and f_i^{eq} are the local equilibrium distribution functions (EDF). The BGK collision operator is governed by the relaxation time τ ($[\tau] = T$).

The variables t and \mathbf{x} are the time and space coordinates, respectively. The velocity set used is the regular two-dimensional nine velocities scheme (D2Q9):

$$\mathbf{c}_i = \begin{cases} (0, 0), & i = 0, \\ (c, 0), (0, c), (-c, 0), (0, -c), & i = 1, \dots, 4, \\ (c, c), (-c, c), (-c, -c), (c, -c), & i = 5, \dots, 8, \end{cases} \quad (2)$$

where c is the lattice speed defined as $c = \Delta x / \Delta t$. The parameters Δx and Δt are the space and time steps.

The specific form of f_i^{eq} ($[f_i^{eq}] = ML^{-3}$) varies depending on the particular method employed. In this work, we use the form:

$$f_i^{eq} = w_i \rho \left(1 + \frac{c_{i\alpha}}{c_s^2} u_\alpha + \frac{c_{i\alpha} c_{i\beta} - c_s^2 \delta_{\alpha\beta}}{2c_s^4} u_\alpha u_\beta \right), \quad (3)$$

where w_i (dimensionless) are the weights associated with each velocity \mathbf{c}_i . For the D2Q9 scheme, these weights are given as $w_0 = 4/9$, $w_{1,2,3,4} = 1/9$, and $w_{5,6,7,8} = 1/36$. The parameter c_s , referred to as the lattice sound speed, is defined as $c/\sqrt{3}$. The variable ρ represents the density, and u_α denotes the fluid velocity.

The term F_i' on the right-hand side of Eq. (1) represents the forcing scheme. This term incorporates the effects of an external volumetric force field F_α ($[F_\alpha] = ML^{-2}T^{-2}$) into the macroscopic conservation equations. Shan and Chen¹¹ introduced an interaction force based on nearest-neighbor interactions (see Shan⁴⁰ for the definition of nearest-neighbor interactions):

$$F_\alpha^{SC} = -G \psi(\mathbf{x}) \sum_{i=1}^8 \omega(|\mathbf{c}_i|^2) \psi(\mathbf{x} + \mathbf{c}_i \Delta t) \frac{c_{i\alpha} \Delta t}{(\Delta t)^2}, \quad (4)$$

where ψ is a density-dependent interaction potential, and G is a parameter that controls the strength of the interaction. The parameters $\omega(|\mathbf{c}_i|^2)$ (dimensionless) are weights, typically set as $\omega(1) = 1/3$ and $\omega(2) = 1/12$. The definition of the interaction potential used in this study follows the approach proposed by Yuan and Schaefer⁴¹, which enables the incorporation of arbitrary equations of state p_{EOS} into the system:

$$\psi(\rho) = \sqrt{\frac{2(p_{EOS} - \rho c_s^2)}{G c^2}} = \sqrt{\frac{2\left(p_{EOS} \frac{(\Delta t)^2}{(\Delta x)^2} - \frac{\rho}{3}\right)}{G}}. \quad (5)$$

When this technique is used, the parameter G no longer controls the interaction strength. Since authors in the literature commonly adopt $p_{EOS} < \rho c_s^2$, we can simply set $G = -1$. If G is defined as a dimensionless quantity, then $[\psi] = [\sqrt{\rho}] = M^{1/2} L^{-3/2}$.

When applying the original force proposed by Shan and Chen¹¹, the pseudo-potential method exhibits certain issues related to thermodynamic consistency and the inability to adjust surface tension. To address these limitations, several approaches were developed⁴²⁻⁴⁵. In this work, we add the terms derived by Czelusniak *et al.*⁴⁶ into the interaction force:

$$F_\alpha^{\text{int}} = F_\alpha^{SC} - \frac{G}{12} \frac{(\Delta x)^4}{(\Delta t)^2} \left(\frac{3}{2} \varepsilon + 2\kappa - 2 \right) M_\beta^{(1)} M_{\alpha\beta}^{(2)} + \frac{G}{6} \frac{(\Delta x)^4}{(\Delta t)^2} (\kappa - 1) M_\alpha^{(1)} M_{\beta\beta}^{(2)}, \quad (6)$$

where ε and κ are adjustable parameters to control phase densities and surface tension. Also, $M_\alpha^{(1)}$ and $M_{\alpha\beta}^{(2)}$ are defined as:

$$M_\alpha^{(1)} = \sum_i w_i \psi(\mathbf{x} + \mathbf{c}_i \Delta t) \frac{c_{i\alpha}}{c_s^2 \Delta t} = \partial_\alpha \psi + O((\Delta x)^2), \quad (7a)$$

$$M_{\alpha\beta}^{(2)} = \sum_i w_i \psi(\mathbf{x} + \mathbf{c}_i \Delta t) \frac{c_{i\alpha} c_{i\beta} - c_s^2 \delta_{\alpha\beta}}{c_s^4 (\Delta t)^2} = \partial_\alpha \partial_\beta \psi + O((\Delta x)^2). \quad (7b)$$

The interaction force can be implemented using various forcing schemes. In this study, we adopt the forcing scheme proposed by Guo and Zhao¹⁴:

$$F_i' = w_i \left(1 - \frac{\Delta t}{2\tau} \right) \left(\frac{c_{i\alpha}}{c_s^2} F_\alpha + \frac{c_{i\alpha} c_{i\beta} - c_s^2 \delta_{\alpha\beta}}{c_s^4} F_\alpha u_\beta \right). \quad (8)$$

Here, the total force F_α is the combination of the interaction force F_α^{int} and other external forces, such as gravity.

The relation between the particle distribution functions f_i and the macroscopic fluid velocity u_α depends on the chosen forcing scheme. For the scheme adopted in this study, the density and velocity fields are defined as follows:

$$\rho = \sum_i f_i, \quad (9a)$$

$$\rho u_\alpha = \sum_i f_i c_{i\alpha} + \frac{F_\alpha \Delta t}{2}. \quad (9b)$$

III. P-LBM PARTIAL DIFFERENTIAL EQUATION

When analyzing the pseudo-potential method's numerical scheme using the third-order analysis proposed by Lycett-Brown and Luo⁴⁵, the following mass and momentum conservation equations are obtained:

$$\partial_t \rho + \partial_\alpha (\rho u_\alpha) = 0, \quad (10a)$$

$$\partial_t (\rho u_\alpha) + \partial_\beta (\rho u_\alpha u_\beta) = -\partial_\beta p_{\alpha\beta} + \partial_\beta \sigma'_{\alpha\beta} + F_{g,\alpha}. \quad (10b)$$

Here, the viscous stress tensor $\sigma'_{\alpha\beta}$ is expressed as:

$$\sigma'_{\alpha\beta} = \rho \nu (\partial_\beta u_\alpha + \partial_\alpha u_\beta). \quad (11)$$

The kinematic viscosity ν , which appear in Eq. (11), is related to the relaxation time by $\nu = c_s^2(\tau - 0.5\Delta t)$.

The effect of the interaction force was incorporated into the pressure tensor $p_{\alpha\beta}$, leaving only the gravitational force $F_{g,\alpha}$ in Eq. (10b). The pressure tensor is expressed as:

$$\begin{aligned} p_{\alpha\beta} = & \left(p_{EOS} - \frac{G}{8} \frac{(\Delta x)^4}{(\Delta t)^2} \varepsilon (\partial_\gamma \psi) (\partial_\gamma \psi) \right. \\ & + \frac{G}{12} \frac{(\Delta x)^4}{(\Delta t)^2} (3 - 2\kappa) \psi \partial_\gamma \partial_\gamma \psi \left. \right) \delta_{\alpha\beta} \quad (12) \\ & + \frac{G}{6} \frac{(\Delta x)^4}{(\Delta t)^2} \kappa \psi \partial_\alpha \partial_\beta \psi. \end{aligned}$$

In the finite-difference literature, these PDEs would be classified as modified equations⁴⁷. It is the differential equation obtained by replacing the numerical approximations in the discrete equation with their Taylor series expansions. The terms retained in the equations above are of the order $(\Delta x)^2$ and $(\Delta t)^2$. A rigorous consistency analysis of the method would require determining the truncation errors, which could be done following the procedure developed by Simonis and Krause⁴⁸. However, we defer this more in-depth theoretical analysis to future work and proceed with our analysis based on modified equations.

The PDE approximated by the P-LBM is grid-dependent, as it relies on Δx and Δt . This dependency manifests in the pressure tensor (Eq. 12) and the interaction potential ψ (Eq. 5). This behavior introduces challenges when discussing the consistency of the P-LBM. By definition, consistency requires that a numerical method approximates a specific PDE. However, in the case of the P-LBM, the PDE varies with each grid resolution.

We proceed to analyze the behavior of the PDE under a diffusive scaling, $\Delta t \propto (\Delta x)^2$. For simplicity, we assume $\Delta t = \sqrt{r}(\Delta x)^2$, where r is a constant. Based on this assumption, the following result is obtained:

$$\lim_{\Delta x \rightarrow 0} \psi = \lim_{\Delta x \rightarrow 0} \sqrt{\frac{2(p_{EOS}(\Delta x)^2 r - \frac{\rho}{3})}{G}} = \sqrt{\frac{2}{3}} \sqrt{\bar{\rho}}. \quad (13)$$

We assume $G = -1$. Consequently, Eq. (12) can be reformulated to express the pressure tensor of the PDE solved by the P-LBM:

$$\begin{aligned} p_{\alpha\beta} = & \left(p_{EOS} + \frac{1}{12r} \varepsilon (\partial_\gamma \sqrt{\bar{\rho}}) (\partial_\gamma \sqrt{\bar{\rho}}) \right. \\ & \left. - \frac{1}{18r} (3 - 2\kappa) \sqrt{\bar{\rho}} \partial_\gamma \partial_\gamma \sqrt{\bar{\rho}} \right) \delta_{\alpha\beta} \quad (14) \\ & - \frac{1}{9r} \kappa \sqrt{\bar{\rho}} \partial_\alpha \partial_\beta \sqrt{\bar{\rho}}. \end{aligned}$$

The presence of the constant r implies that the final pressure tensor remains dependent on the choice of the grid. However, it is possible to compare the results of two simulations under a diffusive scaling refinement, as the pressure tensor remains unchanged. This allows us to determine the convergence order of the method.

The main advantage of expressing the pressure of the P-LBM PDE in the form of Eq. (14), lies in the ability to directly relate the parameters of the pseudopotential method to the physical properties we aim to impose in the simulation (phase densities, interface thickness and surface tension). This will be explored in Section IV.

IV. COMPUTING P-LBM PARAMETERS

Obtaining the limiting PDE of the P-LBM is more than a mere theoretical curiosity. In this section, we demonstrate that through the derived PDE, it is possible to relate the multiphase physical properties (phase densities, interface thickness, and surface tension) to the method's parameters (equation of state parameters, ε and κ). This approach addresses one of the major challenges of the P-LBM: the empirical adjustment of the method parameters to achieve the desired physical properties.

The mechanical stability condition^{40,42} for the P-LBM is given by:

$$\int_{\rho_v}^{\rho_l} (p_{EOS} - p_0) \frac{\psi}{\psi^{1+\varepsilon}} d\rho \propto \int_{\rho_v}^{\rho_l} (p_{EOS} - p_0) \frac{d\rho}{\sqrt{\rho}^{2+\varepsilon}} = 0. \quad (15)$$

This relation becomes equivalent to the Maxwell equal area rule when $\varepsilon = 2$. Throughout the remainder of this work, we assume $\varepsilon = 2$ for the numerical tests.

For this work, we propose the following novel equation of state:

$$\begin{aligned} p_{EOS} = & \frac{p_c}{\rho_c^3} \left[2\rho^3 + (\rho_v - 2\rho_l)\rho^2 - 3\sqrt{\rho_v}\rho^{2.5} \right. \\ & \left. + 2\sqrt{\rho_v}\rho_l\rho^{1.5} + \sqrt{\rho_v}\rho_l^2\rho^{0.5} \right], \quad (16) \end{aligned}$$

where ρ_v , ρ_l , and ρ_c represent the vapor, liquid, and critical densities, respectively. The critical pressure is denoted by p_c . This equation is designed to satisfy the Maxwell construction, with ρ_v and ρ_l as the equilibrium densities. This EOS was proposed because it provides a useful and easy way to link its parameters with macroscopic physical properties.

Next, we want to impose a certain interface thickness ξ . The interface is defined as the region where $\rho_v + 0.33(\rho_l -$

$\rho_v) < \rho < \rho_v + 0.67(\rho_l - \rho_v)$. This can be done by setting p_c/ρ_c^3 according to the following formula:

$$\frac{p_c}{\rho_c^3} = \frac{(f_\xi(\rho_{l;1}) - f_\xi(\rho_{l;2}))^2}{6r\xi^2}, \quad (17)$$

where $\rho_{l;1} = \rho_v + 0.33(\rho_l - \rho_v)$ and $\rho_{l;2} = \rho_v + 0.67(\rho_l - \rho_v)$. The function $f_\xi(\rho)$ is defined as:

$$\begin{aligned} f_\xi(\rho) = & \frac{1}{\rho_l - \rho_v} \ln(\sqrt{\rho} - \sqrt{\rho_v}) \\ & - \frac{1}{2\sqrt{\rho_l}(\sqrt{\rho_l} - \sqrt{\rho_v})} \ln(\sqrt{\rho_l} - \sqrt{\rho}) \\ & - \frac{1}{2\sqrt{\rho_l}(\sqrt{\rho_v} + \sqrt{\rho_l})} \ln(\sqrt{\rho} + \sqrt{\rho_l}). \end{aligned} \quad (18)$$

The theoretical derivation of this expression for the interface thickness is provided in Appendix A.

Finally, the surface tension γ is imposed by computing the parameter κ as:

$$\kappa = \sqrt{\frac{27\rho_c^3}{2r\rho_c} \frac{\gamma}{f_\gamma(\rho_v) - f_\gamma(\rho_l)}}, \quad (19)$$

where:

$$f_\gamma(\rho) = \frac{\rho^2}{4} - \frac{\rho_2}{2}\rho - \frac{\sqrt{\rho_1}}{3}\rho^{1.5} + \sqrt{\rho_1}\rho_2\rho^{0.5}. \quad (20)$$

The theoretical derivation of this expression for surface tension is provided in Appendix B.

The proposed approach does not alter the numerical scheme of the pseudo-potential method, but rather provides a way to link the simulation parameters with the desired physical properties. As a result, the positive features of the method, such as its computational efficiency, are preserved. The pseudo-potential method in the presented formulation is highly efficient, as it uses only one distribution function and a single LBE. Moreover, the interaction force depends only on nearest-neighboring nodes, avoiding costly communication operations between distant lattices²². Thus, one of the appealing aspects of the proposed approach is that it does not add any complexity to the method.

Next, we present details of our OpenLB implementation.

V. IMPLEMENTATIONS IN OPENLB

OpenLB²⁹ is a robust simulation software based on LBM. In this work, we detail how our implementation operates using physical units. To make a clear distinction between units systems we define a generic variable X_{phs} as given in physical units and X_{lat} in lattice units.

First, the user specifies the desired fluid properties in physical units, such as the densities $\rho_{v;phs}$ and $\rho_{l;phs}$, the viscosities $\nu_{v;phs}$ and $\nu_{l;phs}$, and the surface tension γ_{phs} . Additionally, the user defines the geometry of the domain in physical units. For instance, the user may define a characteristic length of the domain L_{phs} .

To enable unit conversion, the multiphase unit converter requires three key inputs in lattice units. These inputs are: the characteristic length L_{lat} , the kinematic viscosity of the liquid phase $\nu_{l;lat}$ and the liquid density $\rho_{l;lat}$. Based on these inputs, the conversion factors for length C_L , time C_T , and mass C_M from lattice to physical units are calculated:

$$C_L = \frac{L_{phs}}{L_{lat}}, \quad C_T = (C_L)^2 \frac{\nu_{l;lat}}{\nu_{l;phs}}, \quad C_M = (C_L)^3 \frac{\rho_{l;phs}}{\rho_{l;lat}}. \quad (21)$$

For a pure hydrodynamic problem (without heat transfer or chemical reactions), these conversion factors are sufficient to convert any physical property. For example, the conversion factors of velocity C_U , volumetric force C_{VF} and surface tension C_γ are obtained as:

$$C_U = \frac{C_L}{C_T}; \quad C_{VF} = \frac{C_M}{C_L^2 C_T^2}; \quad C_\gamma = \frac{C_M}{C_T^2}. \quad (22)$$

It is worth noting that the conversion factor transforms a variable from lattice units to physical units. For example, if U_{phs} is the velocity in physical units and U_{lat} is the velocity in lattice units, they are related by $U_{phs} = C_U U_{lat}$.

After obtaining all properties in lattice units, such as the interface thickness ξ and surface tension γ , Eqs. (17) and (19) are used to compute p_c/ρ_c^3 and κ . The knowledge of r is not required, as $r = 1$ in lattice units. We illustrate our unit converter by presenting a snapshot of our OpenLB code in Fig. 1. The converter also accepts the characteristic physical velocity as an input if the user wishes to calculate and print the Reynolds number.

```
// === 1st Step: Unit Converter ===
MultiPhaseUnitConverterFromRelaxationTime<T,DESCRIPTOR> converter(
(T) N, // resolution
(T) 0.7, // lattice relaxation time
(T) rho_liquid / 1000., // lattice density
(T) L, // charPhysLength
(T) 0., // charPhysVelocity in __m / s__
(T) nu_liquid, // physViscosity in __m^2 / s__
(T) rho_liquid, // physDensity in __kg / m^3__
(T) surfTension // physSurfaceTension in __kg / s__
);

lat_rho_vapor = rho_vapor / converter.getConversionFactorDensity();
lat_rho_liquid = rho_liquid / converter.getConversionFactorDensity();
lat_surfTension = surfTension / converter.getConversionFactorSurfaceTension();
```

FIG. 1. Example of the unit converter implemented in OpenLB, showing the conversion of physical properties into lattice units. This converter allows users to specify fluid properties directly in physical units, simplifying the simulation setup.

The codes used in this work will be available in the next release of OpenLB (1.8), which can be downloaded from the website: <https://www.openlb.net/download/>. Authors can also request the codes by email or through the OpenLB forum: <https://www.openlb.net/forum/>.

VI. RESULTS

In this section, we conduct several benchmark tests and analyze the order of convergence of the numerical method with

Property	Vapor phase	Liquid phase
Density ρ [kg/m ³]	37.5	1187
Kinematic viscosity ν [$\mu\text{m}^2/\text{s}$]	0.339	0.158
Surface tension γ [mN/m]	7.58	

TABLE I. Properties of saturated R134a^{49–51} at $T = 30^\circ\text{C}$.

respect to the analytical solutions. All simulations were performed using R134a as the working fluid. Table I summarizes the fluid properties.

Unless otherwise stated, we set $\tau_{l;lat} = 0.56$ and $\rho_{l;lat} = 1.187$ in lattice units. The choice of a small relaxation time was necessary due to the low viscosity of the fluid. Other parameters are computed using properties in physical units and conversion factors – Eqs. (21) and (22). The relaxation time applied in the LBE is a linear combination between the liquid and vapor relaxation times, τ_l and τ_v :

$$\tau = \tau_v + \frac{\rho - \rho_v}{\rho_l - \rho_v} (\tau_l - \tau_v). \quad (23)$$

To analyze the convergence of the method, we define the numerical solution s_{num} , which is given by a matrix resulting from a simulation and may represent a field of densities, velocities, or other quantities. Based on this, we define the analytical solution as s_{ana} , which represents a matrix containing the values of the analytical solutions at the same points as s_{num} . Finally, the error matrix $e = s_{num} - s_{ana}$ is defined. The relative norms are then computed as follows:

$$\begin{aligned} L_1 &= \frac{\sum |e_{i,j}|}{\sum |s_{ana;i,j}|}, \\ L_2 &= \frac{\sqrt{\sum (e_{i,j})^2}}{\sqrt{\sum (s_{ana;i,j})^2}}, \\ L_\infty &= \frac{\max |e_{i,j}|}{\max |s_{ana;i,j}|}, \end{aligned} \quad (24)$$

where i and j represent the indexes of the elements of e .

In cases where the analytical solution is zero everywhere, such as for spurious currents, we instead define the norms solely in terms of the errors:

$$\begin{aligned} L_1 &= \sum |e_{i,j}|, \\ L_2 &= \sqrt{\sum (e_{i,j})^2}, \\ L_\infty &= \max |e_{i,j}|. \end{aligned} \quad (25)$$

Before describing the tests performed, we provide some comments regarding the scales of the selected problems. We chose problems with characteristic lengths on the order of $10 \mu\text{m}$. Although problems can be simulated on larger scales, the time conversion factor C_T increases proportionally to C_L^2 (21), which in turn leads to a reduction in the surface tension conversion factor C_γ (22). To recover the correct physical surface tension, it would be necessary to simulate larger

surface tension values in lattice units. This can be achieved by increasing the parameter κ (6) or by reducing the relaxation time to decrease C_T .

However, since we are using the BGK collision operator, there is a lower bound on how much we can reduce τ , limiting our ability to adjust C_T freely. We explore the variation of κ in the droplet test. For this reason, we opted to work with problems at a relatively small physical scale. We intend to explore problems at different scales in future work.

A. Planar interface

The first benchmark is the planar interface test problem. Although simple, this test is used here to demonstrate the validity of the equations presented in Section IV, particularly regarding the ability to directly prescribe the interface thickness within the method. A schematic of the test geometry is shown in Fig. (2), where $L_x = 10 \mu\text{m}$, $L_y = 0.5 \mu\text{m}$ and $L_I = 5 \mu\text{m}$. Periodic boundary conditions are applied and the simulation is carried out until equilibrium.

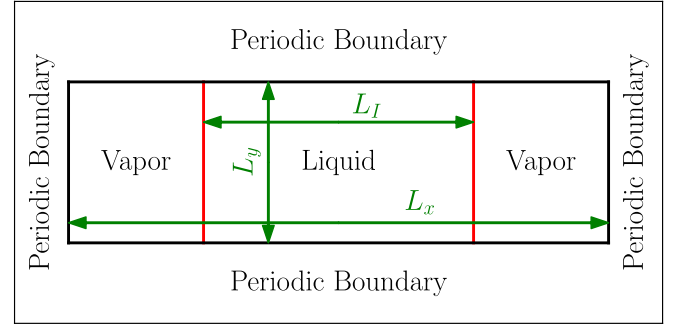


FIG. 2. Schematic diagram of the planar interface test configuration. The geometry consists of a two-dimensional domain ($L_x \times L_y$), where the liquid phase occupies a central region of length L_I , surrounded by vapor. Periodic conditions are applied to all boundaries.

The simulation is carried out using five different grid resolutions, and all the necessary information to reproduce the test is shown in Table II.

-	Grid 1	Grid 2	Grid 3	Grid 4	Grid 5
N_x	100	200	300	400	500
N_y	5	10	15	20	25
Δx [nm]	100	50	33.3	25	20
Δt [ps]	1266	316.4	140.7	79.11	50.63
ξ [m]	$1.5\Delta x$	$3.0\Delta x$	$4.5\Delta x$	$6.0\Delta x$	$7.5\Delta x$
C_U [m/s per l.u.]	79	158	237	316	395
C_γ [N/m per l.u.]	0.62	1.25	1.87	2.50	3.12

TABLE II. Discretization parameters of planar interface test case. N_x and N_y are the number of grid nodes used to discretize the domain. Δx (in nanometers) is defined as L_x/N_x . Δt (in picoseconds) is the time step and ξ is the interface thickness. C_U and C_γ are the conversion factors from lattice units (l.u.) to physical units for velocity and surface tension – Eq. (22).

The simulation results are presented in Fig. 3. The entire density profile was compared with the analytical solution Eq. (A6) in Appendix A. The error norms converge with second order of accuracy.

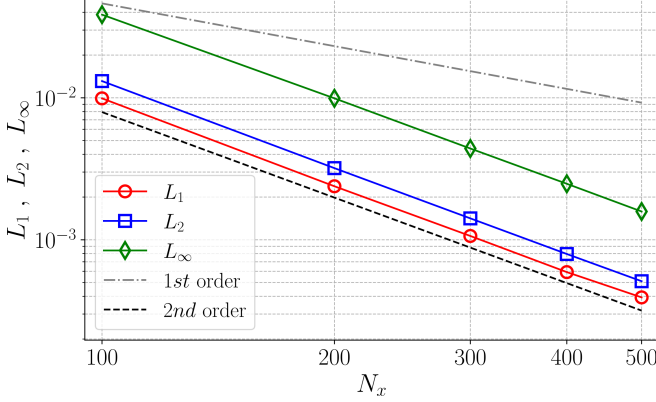


FIG. 3. Comparison of the L_1 , L_2 , and L_∞ norm errors between the numerical simulation and the analytical solution for the planar interface test. The norms are defined in Eq. (24). Norms are plotted as a function of number of grid points in x -direction N_x .

Fig. (4) shows the density profile along the interface for the coarser mesh ($N_x = 100$) and the finer mesh ($N_x = 500$). It is observed that for the coarser mesh, there was a small difference compared to the analytical solution. However, the finer mesh coincides with the reference solution with high accuracy.

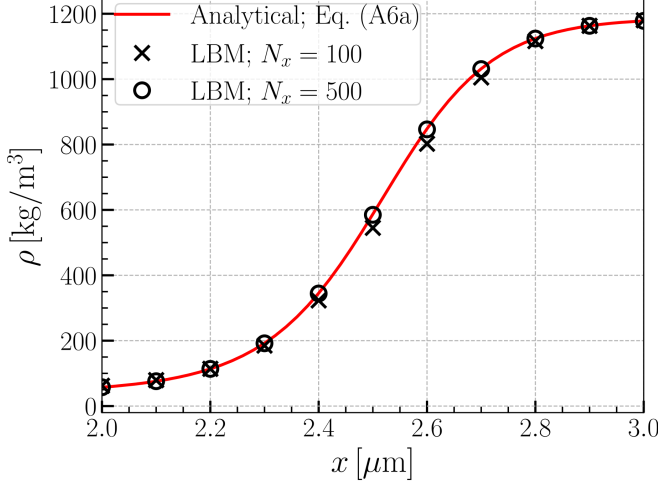


FIG. 4. Density profile ρ along the interface region (aligned with the x -axis) for the planar interface test. The plot compares analytical and numerical results at different resolutions, denoted by N_x .

B. Static droplet

The second test is the static drop test, where a liquid droplet is placed in the middle of a 2D cuboid domain of dimensions

$L_x = 15 \mu\text{m}$ and $L_y = 15 \mu\text{m}$, surrounded by vapor, as shown in Fig. 5. Periodic boundary conditions are applied.

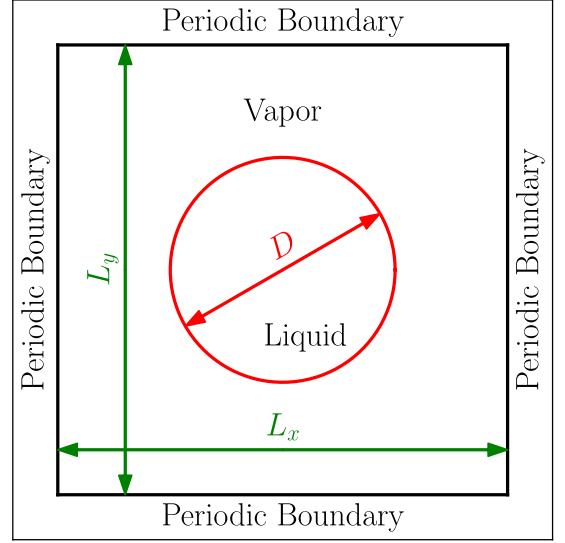


FIG. 5. Schematic diagram of the static droplet test configuration. A two-dimensional domain ($L_x \times L_y$) contains a liquid droplet of diameter D placed at the center, surrounded by vapor. Periodic boundary conditions are applied in all directions.

First, we assess whether the surface tension reproduced by the method matches the one prescribed by Eq. (19). To this end, we carry out Young-Laplace test by simulating varying droplet diameters.

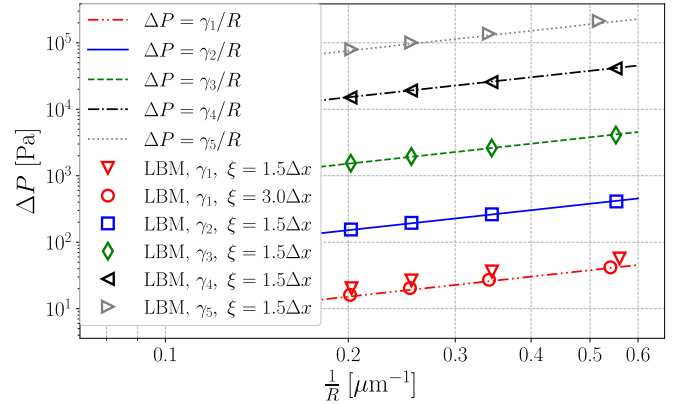


FIG. 6. Laplace pressure ΔP (in Pascal) as a function of droplet curvature $1/R$ for different surface tensions $\gamma_1 = 0.0758 \text{ mN/m}$, $\gamma_2 = 0.758 \text{ mN/m}$, $\gamma_3 = 7.58 \text{ mN/m}$, $\gamma_4 = 75.8 \text{ mN/m}$ and $\gamma_5 = 379 \text{ mN/m}$. Comparison between Young-Laplace relation and LBM results using different interface thickness ξ .

When simulating R134a ($\gamma_3 = 7.58 \text{ mN/m}$) using a discretization of $\Delta x = 0.1 \mu\text{m}$ and $\Delta t = 1.26 \text{ ns}$, the parameter κ obtained from Eq. (19) has a value of 1.026. For values close to one, the term responsible for modifying the surface tension in Eq. (6) tends to zero, indicating that the surface tension is primarily determined by the Shan-Chen force. The results for this case, with $\xi = 1.5\Delta x$, are shown in Fig. 6. Even with

a small ξ , the numerical Laplace pressures are very close to the expected values, indicating that the correct surface tension was imposed.

To test the validity of the proposed approach, we consider surface tensions different from that of R134a. We first test $\gamma_2 = 0.758$ mN/m, which is 100 times smaller than the surface tension of water. Instead of changing κ , we employ an alternative strategy to adjust the surface tension: increasing $\tau_{i,\text{lat}}$ from 0.56 to 0.68. Due to the unit conversion in Eq. (21), this change enables the simulation of the new surface tension while yielding $\kappa = 0.923$, which remains close to one. Figure 6 shows that the results are very good even with $\xi = 1.5\Delta x$. The same approach was applied to simulate $\gamma_4 = 75.8$ mN/m, which is close to the surface tension of water. In this case, we decrease $\tau_{i,\text{lat}}$ to 0.52, resulting in $\kappa = 1.140$. The simulation results were also in close agreement with the imposed surface tension.

Finally, we test two additional cases: $\gamma_1 = 0.0758$ mN/m (with $\tau_{i,\text{lat}} = 0.68$) and $\gamma_5 = 379$ mN/m (with $\tau_{i,\text{lat}} = 0.52$). Instead of further modifying the relaxation time as in the previous cases, we directly adjust κ to 0.0923 for the first case and 5.698 for the second. As shown in Fig. 6, the simulations with $\xi = 1.5\Delta x$ approximate the target surface tensions, but with less accuracy compared to the cases where κ is close to one. This suggests that large changes in κ introduce numerical errors. We repeated the simulation of γ_1 using a higher resolution with $\Delta x = 0.05$ μm , $\Delta t = 0.95$ ns, and $\xi = 3\Delta x$. The finer grid shows better agreement with the desired surface tension in Fig. 6, demonstrating the robustness of the proposed approach for imposing surface tension. As a final remark, we attempted to simulate a surface tension of $\gamma_5 = 758$ mN/m, but the simulation became unstable due to the high value of κ .

An important difference between this test and the planar interface test is the presence of curvature in the interface, which leads to spurious currents caused by discretization errors. In this case, we assess the impact of increasing the computational mesh resolution on spurious currents. To this end, we fix $D = 5\mu\text{m}$ and $\tau_{i,\text{lat}} = 0.62$, and simulate five different meshes, with all relevant data presented in Table III.

-	Grid 1	Grid 2	Grid 3	Grid 4	Grid 5
N_x	100	200	300	400	500
N_y	100	200	300	400	500
Δx [nm]	100	50	33.3	25	20
Δt [ns]	2.532	0.633	0.281	0.158	0.101
ξ [m]	$1.5\Delta x$	$3.0\Delta x$	$4.5\Delta x$	$6.0\Delta x$	$7.5\Delta x$
C_U	39.5	79	118.5	158	197.5
C_γ	0.156	0.312	0.468	0.624	0.780

TABLE III. Discretization parameters of static droplet test case. N_x and N_y are the number of grid nodes used to discretize the domain. Δx (in nanometers) is defined as L_x/N_x . Δt (in nanoseconds) is the time step and ξ is the interface thickness. C_U and C_γ are the conversion factors from lattice units (*l.u.*) to physical units for velocity and surface tension – Eq. (22).

The simulation results are presented in Fig. 7. Norms are computed from the velocity magnitude field using Eq. (25)

since no spurious currents should be observed in reality. The error norms converge with second order of accuracy.

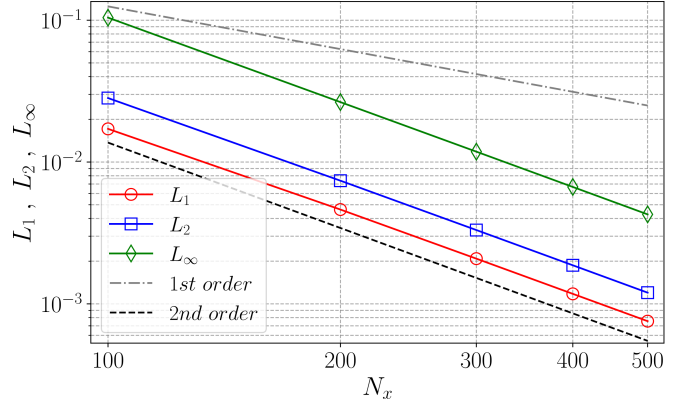


FIG. 7. Comparison of the L_1 , L_2 , and L_∞ norm errors for the static droplet test. The norms, defined in Eq. (25), are computed from the velocity magnitude field.

The simulation with the coarse grid ($N_x = 100$), resulted in a maximum spurious currents magnitude of 0.1 m/s and 2.6×10^{-3} lattice units. With the finest resolution this magnitude decreased to 4.3×10^{-3} m/s and 2.2×10^{-5} in lattice units. It is observed that the velocity in physical units converges with second-order accuracy, while the velocity in lattice units converges to zero with third-order accuracy. This occurs because the conversion factor C_U increases linearly with the grid resolution.

It is important to mention that there are numerical schemes designed to eliminate the presence of spurious currents, such as well-balanced scheme⁵² In this work, we employ a discretization that still exhibits spurious currents; however, our intention is to demonstrate the method's order of convergence through mesh refinement.

C. Galilean invariance

In this section, we describe a test used to evaluate whether the P-LBM respects Galilean invariance. This test is similar to the flat interface test; however, here we introduce a constant velocity U_x throughout the fluid. If the method respects Galilean invariance, the velocity profile should remain constant throughout the simulation. We can consider the fluid to be static relative to an inertial reference frame moving with velocity U_x ; thus, the results of this simulation should not differ from those of the flat interface test. However, due to discretization errors, the method may exhibit a deviation from this behavior.

The configuration of this problem is identical to the flat interface described in Fig. 2. Also, simulation parameters are equal to the ones shown in Table II with the addition of the velocity $U_x = 0.1$ m/s. The simulation begins with zero velocity until $t = 7.91$ μs seconds, allowing the interface density profile to reach equilibrium. A force field is then applied to abruptly change the system's velocity to U_x . The simulation

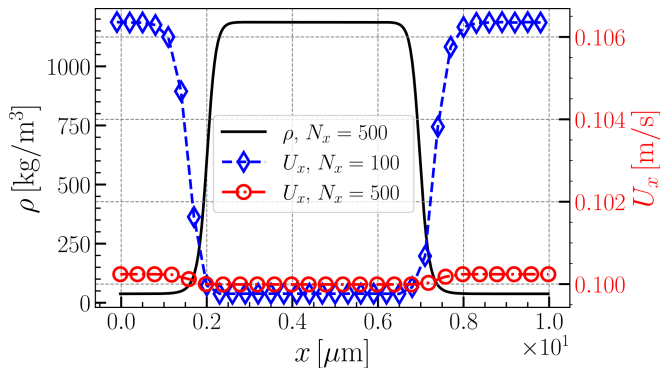


FIG. 8. LBM results for Galilean invariance test. Left axis: Density profile ρ along x -axis. Right axis: Velocity profile U_x along x -axis. Comparison between two grid resolutions $N_x = 100$ and $N_x = 500$.

continues until $t = 31.6 \mu\text{s}$, and the results are recorded.

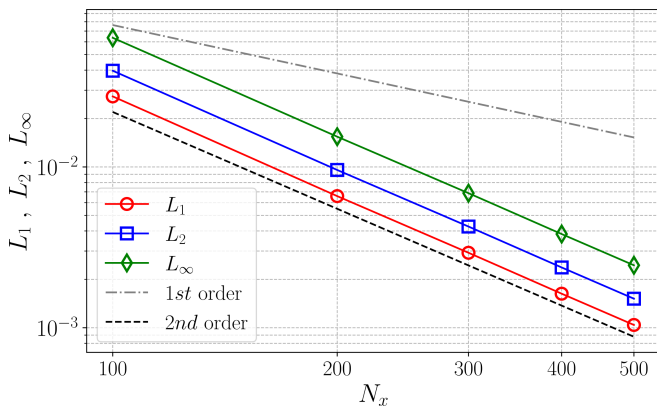


FIG. 9. Errors in the L_1 , L_2 , and L_∞ norms for the Galilean invariance test. The configuration includes a planar interface subjected to a constant velocity field ($U_x = 0.1 \text{ m/s}$).

To illustrate this behavior, we compare the simulation results for $N_x = 100$ and $N_x = 500$ in Fig. 9. The fluid velocity is expected to remain constant throughout the domain, but it is observed that the vapor and liquid phases exhibit a relative velocity. This relative motion between phases persists over time, indicating that it is not a transient phenomenon, but rather a consequence of discretization errors acting at the interface. This highlights the importance of mesh convergence analysis to ensure that such effects do not influence the simulation results.

The error norms are presented in Fig. 9. The norms are given by Eq. (24) and are computed from the velocity field. The analytical solution is simply a constant field with magnitude U_x . The error norms converge with second order of accuracy.

D. Two phase flow between parallel plates

The last test is the two-phase flow between parallel plates. A schematic describing the geometry of the simulation is

shown in Fig. 10. Again, a 2D cuboid geometry with dimensions $L_x = 0.5 \mu\text{m}$ and $L_y = 10 \mu\text{m}$ is defined. Periodic boundary conditions are applied to the side boundaries, while solid walls are applied to the lower and upper boundaries. The bottom part of the domain is filled with liquid, while the upper part is filled with vapor. A volumetric force $F_x = 10^6 \text{ N/m}^3$ is applied in the entire domain to drive the flow.

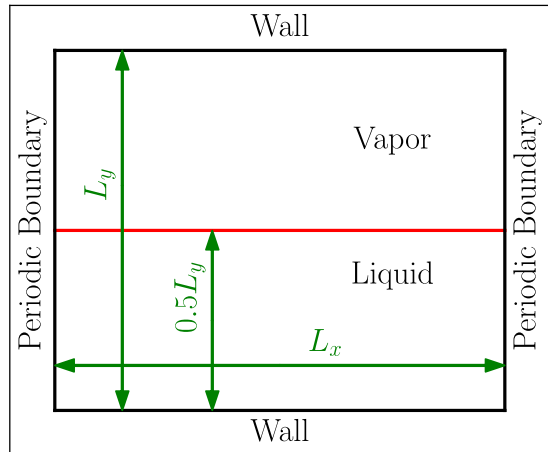


FIG. 10. Schematic diagram of the two-phase flow test between parallel plates. A two-dimensional domain ($L_x \times L_y$) features solid walls at the top and bottom boundaries and periodic boundary conditions on the sides. The lower part contains liquid, while the upper part contains vapor.

Since periodic boundary conditions are applied to the side boundaries, it is not necessary to have a long domain length. Therefore, we choose $L_x < L_y$ to save computational time. Five grid resolutions are tested and parameters are provided in Table IV.

-	Grid 1	Grid 2	Grid 3	Grid 4	Grid 5
N_x	5	10	15	20	25
N_y	100	200	300	400	500
Δx [nm]	100	50	33.3	25	20
Δt [ps]	1266	316.4	140.7	79.11	50.63
ξ [m]	$1.5\Delta x$	$3.0\Delta x$	$4.5\Delta x$	$6.0\Delta x$	$7.5\Delta x$
C_U [m/s per l.u.]	79	158	237	316	395
C_{VF} [TN/m^3 per l.u.]	62.41	499.3	1685	3994	7801
C_γ [N/m per l.u.]	0.62	1.25	1.87	2.50	3.12

TABLE IV. Discretization parameters of two phase flow between parallel plates test. N_x and N_y are the number of grid nodes used to discretize the domain. Δx (in nanometers) is defined as L_x/N_x . Δt (in picoseconds) is the time step and ξ is the interface thickness. C_U , C_{VF} and C_γ are the conversion factors from lattice units (l.u.) to physical units for velocity, volumetric force and surface tension – Eq. (22).

The simulation results are presented in Fig. 11. The norms are given by Eq. (24) and are computed from the velocity field. Similarly to the previous tests, the error norms converge with second order of accuracy.

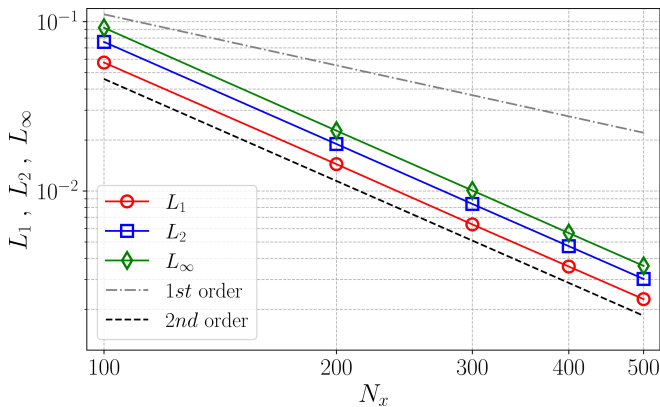


FIG. 11. Errors in the L_1 , L_2 , and L_∞ norms for the two-phase flow test between parallel plates. The norms were computed from Eq. (24) using the velocity field.

To illustrate the simulation results, we plot both the numerical solution (with two grid resolutions) and the analytical solution in Fig. 12. As shown, the highest resolution closely matches the analytical results.

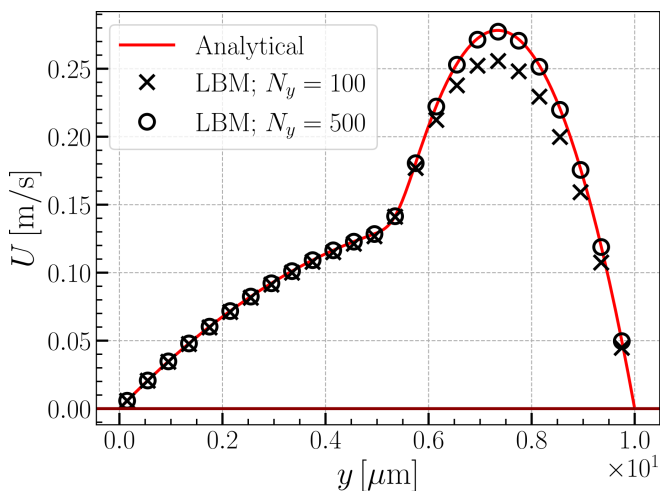


FIG. 12. Velocity profile U along the channel height (aligned with the y -axis) for the two-phase flow test. The plot compares analytical and numerical results at different resolutions, denoted by N_y .

VII. CONCLUSION

In this study, we analyzed the consistency of the P-LBM, focusing on its relationship with macroscopic properties and the PDE it approximates. We derived a formulation that directly links the method parameters to physical properties such as phase densities, interface thickness, and surface tension. This approach eliminates the need for empirical parameter tuning, thereby simplifying the application of the method and improving its robustness.

Furthermore, we implemented and validated our approach in OpenLB, introducing a dedicated unit converter for multi-

phase problems. The benchmarks conducted—including the planar interface, static droplets, Galilean invariance, and two-phase flow between parallel plates—demonstrated second-order convergence and confirmed the numerical consistency of the method. All tests were performed using R134a as working fluid with all properties given in SI units.

The tests performed show that numerical errors occur in multiphase simulations with P-LBM. Therefore, it is important to perform a mesh study to ensure that the numerical errors converge to an acceptable value and to guarantee the reliability of the simulation.

The results obtained not only validate the proposed methodology but also emphasize its potential for future applications in complex and realistic multiphase simulations. The methodology offers a practical approach to applying the pseudo-potential, enabling users to utilize the method more effectively with real simulation parameters.

ACKNOWLEDGMENTS

We acknowledge the support of the Alexander von Humboldt Foundation in sponsoring the postdoctoral fellowship of researcher Dr. Luiz Eduardo Czelusniak at LBRG, KIT.

AUTHORS DECLARATIONS

Conflict of Interest

The authors have no conflicts to disclose.

Data Availability Statement

The data that support the findings of this study are available from the corresponding author upon reasonable request. In addition, the codes used in this work will be available in the next release of OpenLB (1.8), which can be downloaded from the website: <https://www.openlb.net/download/>.

Appendix A: Interface profile

In the following analysis, two fluids separated by a flat interface at equilibrium are considered. Density gradients exist only along the x -axis. The component p_{xx} of the pressure tensor, Eq. (12), can be written as:

$$p_{xx} = p_{EOS} + \frac{1}{6r} \left[\left(\frac{d\sqrt{\rho}}{dx} \right)^2 - \sqrt{\rho} \frac{d^2\sqrt{\rho}}{dx^2} \right]. \quad (\text{A1})$$

Here we consider $\varepsilon = 2$ as discussed in Section IV.

To further simplify the equation, we define $z = d\sqrt{\rho}/dx$. Next, we assume that z is a function of ρ to apply the following transformation:

$$\rho^2 \frac{d}{d\rho} \left(\frac{z^2}{\rho} \right) = - \left(\frac{d\sqrt{\rho}}{dx} \right)^2 + \sqrt{\rho} \frac{d^2\sqrt{\rho}}{dx^2}. \quad (\text{A2})$$

Then, we arrive at the following ordinary differential equation:

$$\frac{d}{d\rho} \left(\frac{z^2}{\rho} \right) = 6r \frac{p_{EOS} - p_{xx}}{\rho^2}. \quad (\text{A3})$$

From Eq. (10b) we notice $p_{xx} = \text{constant}$ for a static planar interface in equilibrium. Also, we have the boundary conditions $p_{xx} = p_{EOS}(\rho_v) = p_{EOS}(\rho_l)$.

Eq. (A3) - together with the EOS of Eq. (16) and the assigned boundary conditions have the following solution:

$$z = -\sqrt{\frac{6rp_c}{\rho_c^3}} (\sqrt{\rho} - \sqrt{\rho_v})(\rho - \rho_l), \quad (\text{A4})$$

with $z = d\sqrt{\rho}/dx$. This equation can also be written as:

$$\sqrt{\frac{6rp_c}{\rho_c^3}} dx = -\frac{d\sqrt{\rho}}{(\sqrt{\rho} - \sqrt{\rho_v})(\rho - \rho_l)}. \quad (\text{A5})$$

Integrating this equation, we obtain:

$$\sqrt{\frac{6rp_c}{\rho_c^3}} x + C_0 = f_\xi(\rho), \quad (\text{A6a})$$

where C_0 is an integration constant and:

$$\begin{aligned} f_\xi(\rho) &= \frac{1}{\rho_l - \rho_v} \ln(\sqrt{\rho} - \sqrt{\rho_v}), \\ &- \frac{1}{2\sqrt{\rho_l}(\sqrt{\rho_l} - \sqrt{\rho_v})} \ln(\sqrt{\rho_l} - \sqrt{\rho}), \\ &- \frac{1}{2\sqrt{\rho_l}(\sqrt{\rho_v} + \sqrt{\rho_l})} \ln(\sqrt{\rho} + \sqrt{\rho_l}). \end{aligned} \quad (\text{A6b})$$

We define the interface width ξ as the distance where $\rho_v + 0.33(\rho_l - \rho_v) < \rho < \rho_v + 0.67(\rho_l - \rho_v)$. Then:

$$\xi = \sqrt{\frac{\rho_c^3}{6rp_c}} (f_\xi(\rho_{l;1}) - f_\xi(\rho_{l;2})), \quad (\text{A7})$$

where $\rho_{l;1} = \rho_v + 0.33(\rho_l - \rho_v)$ and $\rho_{l;2} = \rho_v + 0.67(\rho_l - \rho_v)$.

Appendix B: Surface tension

The surface tension in diffuse interface models for a planar interface case is defined as⁵³:

$$\gamma = \int_{-\infty}^{+\infty} (p_{xx} - p_{yy}) dx, \quad (\text{B1})$$

where x and y represents the normal and tangential directions in respect to the interface. Considering the pressure tensor expression - Eq. (12) - we have the formula:

$$\gamma = -\frac{\kappa}{9r} \int_{-\infty}^{+\infty} \sqrt{\rho} \frac{d^2 \sqrt{\rho}}{dx^2} dx. \quad (\text{B2})$$

Using integral by part, we rewrite the above expression:

$$\gamma = \frac{\kappa}{9r} \left(-\sqrt{\rho} \frac{d\sqrt{\rho}}{dx} \Big|_{-\infty}^{+\infty} + \int_{-\infty}^{+\infty} \left(\frac{d\sqrt{\rho}}{dx} \right)^2 dx \right). \quad (\text{B3})$$

The interface density is constant at the bulk phases meaning $d\sqrt{\rho}/dx = 0$ for $x = \pm\infty$. Then, we write the final form for the expression:

$$\gamma = \frac{\kappa}{9r} \int_{\rho_v}^{\rho_l} \frac{d\sqrt{\rho}}{dx} d\sqrt{\rho}. \quad (\text{B4})$$

We already know the expression for $d\sqrt{\rho}/dx$ which is equal to $z(\rho)$ in Eq. (A4). Then, the surface tension is simply obtained by integration:

$$\gamma = \sqrt{\frac{2rp_c}{27\rho_c^3}} \kappa (f_\gamma(\rho_v) - f_\gamma(\rho_l)). \quad (\text{B5})$$

with:

$$f_\gamma(\rho) = \frac{\rho^2}{4} - \frac{\rho_l}{2} \rho - \frac{\sqrt{\rho_v}}{3} \rho^{1.5} + \sqrt{\rho_v} \rho_l \rho^{0.5}. \quad (\text{B6})$$

¹S. Gong and P. Cheng, "Lattice Boltzmann simulation of periodic bubble nucleation, growth and departure from a heated surface in pool boiling," *International Journal of Heat and Mass Transfer* **64**, 122–132 (2013), DOI: 10.1016/j.ijheatmasstransfer.2013.03.058.

²Q. Li, Q. Kang, M. M. Francois, Y. He, and K. Luo, "Lattice Boltzmann modeling of boiling heat transfer: The boiling curve and the effects of wettability," *International Journal of Heat and Mass Transfer* **85**, 787–796 (2015), DOI: 10.1016/j.ijheatmasstransfer.2015.01.136.

³H. Cao, Q. Zuo, Q. An, Z. Zhang, H. Liu, and D. Zhang, "Lattice Boltzmann method for simulation of solid–liquid conjugate boiling heat transfer surface with mixed wettability structures," *Physics of Fluids* **34** (2022), DOI: 10.1063/5.0087644.

⁴D.-V. Le, J. Li, H. Li, L.-S. Pan, M. Cheng, X. Zhang, C.-W. Kang, and J. Lou, "Improved boundary conditions for lattice Boltzmann modeling of pool boiling at low temperature," *Physics of Fluids* **35** (2023), DOI: 10.1063/5.0142155.

⁵T. Alsadik, S. W. Welch, and K. N. Premnath, "Lattice Boltzmann simulations of quasi-steady film and axisymmetric nucleate boiling," *Physics of Fluids* **36**, 033355 (2024), DOI: 10.1063/5.0192074.

⁶V. Heuveline, M. J. Krause, and J. Latt, "Towards a hybrid parallelization of lattice Boltzmann methods," *Computers & Mathematics with Applications* **58**, 1071–1080 (2009), DOI: 10.1016/j.camwa.2009.04.001.

⁷T. Henn, G. Thäter, W. Dörfler, H. Nirschl, and M. J. Krause, "Parallel dilute particulate flow simulations in the human nasal cavity," *Computers & Fluids* **124**, 197–207 (2016), DOI: 10.1016/j.compfluid.2015.08.002.

⁸J. E. Marquardt, N. Hafen, and M. J. Krause, "A novel particle decomposition scheme to improve parallel performance of fully resolved particulate flow simulations," *Journal of Computational Science* **78**, 102263 (2024), DOI: 10.1016/j.jocs.2024.102263.

⁹P. Cheng, N. Gui, X. Yang, JiyuanTu, and S. Jiang, "Application of lattice Boltzmann methods for the multiphase fluid pipe flow on graphical processing unit," *The Journal of Computational Multiphase Flows* **10**, 109–118 (2018), DOI: 10.1177/1757482X17746922.

¹⁰G. Yang, Y. Chen, S. Chen, and M. Wang, "Implementation of a direct-addressing based lattice Boltzmann GPU solver for multiphase flow in porous media," *Computer Physics Communications* **291**, 108828 (2023), DOI: 10.1016/j.cpc.2023.108828.

¹¹X. Shan and H. Chen, "Lattice Boltzmann model for simulating flows with multiple phases and components," *Physical Review E* **47**, 1815 (1993), DOI: 10.1103/PhysRevE.47.1815.

- ¹²X. Shan and H. Chen, “Simulation of nonideal gases and liquid-gas phase transitions by the lattice Boltzmann equation,” *Physical Review E* **49**, 2941 (1994), DOI: 10.1103/PhysRevE.49.2941.
- ¹³M. R. Swift, E. Orlandini, W. Osborn, and J. Yeomans, “Lattice Boltzmann simulations of liquid-gas and binary fluid systems,” *Physical Review E* **54**, 5041 (1996), DOI: 10.1103/PhysRevE.54.5041.
- ¹⁴Z. Guo and T. Zhao, “Lattice Boltzmann model for incompressible flows through porous media,” *Physical Review E* **66**, 036304 (2002), DOI: 10.1103/PhysRevE.66.036304.
- ¹⁵X. He, S. Chen, and R. Zhang, “A lattice Boltzmann scheme for incompressible multiphase flow and its application in simulation of Rayleigh–Taylor instability,” *Journal of Computational Physics* **152**, 642–663 (1999), DOI: 10.1006/jcph.1999.6257.
- ¹⁶T. Lee and C.-L. Lin, “A stable discretization of the lattice Boltzmann equation for simulation of incompressible two-phase flows at high density ratio,” *Journal of Computational Physics* **206**, 16–47 (2005), DOI: 10.1016/j.jcp.2004.12.001.
- ¹⁷H. Liang, J. Xu, J. Chen, H. Wang, Z. Chai, and B. Shi, “Phase-field-based lattice Boltzmann modeling of large-density-ratio two-phase flows,” *Physical Review E* **97**, 033309 (2018), DOI: 10.1103/PhysRevE.97.033309.
- ¹⁸D. H. Rothman and J. M. Keller, “Immiscible cellular-automaton fluids,” *Journal of Statistical Physics* **52**, 1119–1127 (1988), DOI: 10.1007/BF01019743.
- ¹⁹A. K. Gunstensen, D. H. Rothman, S. Zaleski, and G. Zanetti, “Lattice Boltzmann model of immiscible fluids,” *Physical Review A* **43**, 4320 (1991), DOI: 10.1103/PhysRevA.43.4320.
- ²⁰Z. Qin, J. Zhu, W. Chen, C. Li, and B. Wen, “An effective pseudo-potential lattice Boltzmann model with extremely large density ratio and adjustable surface tension,” *Physics of Fluids* **34**, 113328 (2022).
- ²¹Y. Zhao, G. G. Pereira, S. Kuang, Z. Chai, and B. Shi, “A pseudopotential lattice Boltzmann analysis for multicomponent flow,” *Communications in Computational Physics* **32**, 1156–1178 (2022), DOI: 10.4208/cicp.OA-2022-0209.
- ²²L. E. Czelusniak, I. T. Martins, L. C. Gómez, N. A. V. Bulgarelli, W. M. Verde, and M. S. de Castro, “Fundamental comparison between the pseudopotential and the free energy lattice Boltzmann methods,” *Physica A: Statistical Mechanics and its Applications* **660**, 130374 (2025), DOI: 10.1016/j.physa.2025.130374.
- ²³K. Pasieczynski and B. Chen, “Fluid–fluid interactions in pseudopotential lattice Boltzmann models: Effects of model schemes and fluid properties,” *International Journal for Numerical Methods in Fluids* **93**, 1578–1605 (2021), DOI: 10.1002/ffd.4943.
- ²⁴S.-C. Wang, Z.-X. Tong, Y.-L. He, and X. Liu, “Unit conversion in pseudopotential lattice Boltzmann method for liquid–vapor phase change simulations,” *Physics of Fluids* **34** (2022), DOI: 10.1063/5.0106079.
- ²⁵S. S. Baakeem, S. A. Bawazeer, and A. A. Mohamad, “A novel approach of unit conversion in the lattice Boltzmann method,” *Applied Sciences* **11**, 6386 (2021), DOI: 10.3390/app11146386.
- ²⁶A. Jaramillo, V. P. Mapelli, and L. Cabezas-Gómez, “Pseudopotential lattice Boltzmann method for boiling heat transfer: A mesh refinement procedure,” *Applied Thermal Engineering* **213**, 118705 (2022), DOI: 10.1016/j.applthermaleng.2022.118705.
- ²⁷W. Zheng, F. Hong, and S. Gong, “Improved multi-relaxation time thermal pseudo-potential lattice Boltzmann method with multi-block grid and complete unit conversion for liquid–vapor phase transition,” *Physics of Fluids* **35** (2023), DOI: 10.1063/5.0147074.
- ²⁸H. Oh and H. Jo, “Turbulent flow boiling simulation based on pseudopotential lattice Boltzmann method with developed wall boundary treatments and unit conversion,” *Applied Thermal Engineering* **248**, 123148 (2024), DOI: 10.1016/j.applthermaleng.2024.123148.
- ²⁹M. J. Krause, A. Kummerländer, S. J. Avis, H. Kusumaatmaja, D. Dapelo, F. Klemens, M. Gaedtke, N. Hafen, A. Mink, R. Trunk, J. E. Marquardt, M.-L. Maier, M. Haussmann, and S. Simonis, “OpenLB–Open source lattice Boltzmann code,” *Computers & Mathematics with Applications* (2020), DOI: 10.1016/j.camwa.2020.04.033.
- ³⁰A. Kummerländer, T. Bingert, F. Bukreev, L. E. Czelusniak, D. Dapelo, N. Hafen, M. Heinzlmann, S. Ito, J. Jeßberger, H. Kusumaatmaja, J. E. Marquardt, M. Rennick, T. Pertz, F. Prinz, M. Sadric, M. Schecher, S. Simonis, P. Sitter, D. Teutscher, M. Zhong, and M. J. Krause, “OpenLB Release 1.7: Open Source Lattice Boltzmann Code,” (2024), DOI: 10.5281/zenodo.10684609.
- ³¹F. Bukreev, F. Raichle, H. Nirschl, and M. J. Krause, “Simulation of adsorption processes on moving particles based on an Euler-Euler description using a lattice Boltzmann discretization,” *Chemical Engineering Science* **270**, 118485 (2023), DOI: 10.1016/j.ces.2023.118485.
- ³²N. Hafen, J. E. Marquardt, A. Dittler, and M. J. Krause, “Simulation of particulate matter structure detachment from surfaces of wall-flow filters for elevated velocities applying lattice Boltzmann methods,” *Fluids* **8**, 99 (2023), DOI: 10.3390/fluids8030099.
- ³³M. Siodlaczek, M. Gaedtke, S. Simonis, M. Schweiker, N. Homma, and M. J. Krause, “Numerical evaluation of thermal comfort using a large eddy lattice Boltzmann method,” *Building and Environment* **192**, 107618 (2021), DOI: 10.1016/j.buildenv.2021.107618.
- ³⁴S. Simonis, D. Oberle, M. Gaedtke, P. Jenny, and M. J. Krause, “Temporal large eddy simulation with lattice Boltzmann methods,” *Journal of Computational Physics* **454**, 110991 (2022), DOI: 10.1016/j.jcp.2022.110991.
- ³⁵F. Reinke, N. Hafen, M. Haussmann, M. Novosel, M. J. Krause, and A. Dittler, “Applied Geometry Optimization of an Innovative 3D-Printed Wet-Scrubber Nozzle with a Lattice Boltzmann Method,” *Chemie Ingenieur Technik* **94**, 348–355 (2022), DOI: 10.1002/cite.202100151.
- ³⁶J. Jeßberger, J. E. Marquardt, L. Heim, J. Mangold, F. Bukreev, and M. J. Krause, “Optimization of a micromixer with automatic differentiation,” *Fluids* **7**, 144 (2022), DOI: 10.3390/fluids7050144.
- ³⁷F. Bukreev, S. Simonis, A. Kummerländer, J. Jeßberger, and M. J. Krause, “Consistent lattice Boltzmann methods for the volume averaged Navier–Stokes equations,” *Journal of Computational Physics* **490**, 112301 (2023), DOI: 10.1016/j.jcp.2023.112301.
- ³⁸S. Simonis, J. Nguyen, S. J. Avis, W. Dörfler, and M. J. Krause, “Binary fluid flow simulations with free energy lattice Boltzmann methods,” *Discrete and Continuous Dynamical Systems-S* **17**, 3278–3294 (2024), DOI: 10.3934/dcdss.2023069.
- ³⁹P. L. Bhatnagar, E. P. Gross, and M. Krook, “A model for collision processes in gases. I. Small amplitude processes in charged and neutral one-component systems,” *Physical Review* **94**, 511 (1954), DOI: 10.1103/PhysRev.94.511.
- ⁴⁰X. Shan, “Pressure tensor calculation in a class of nonideal gas lattice Boltzmann models,” *Physical Review E* **77**, 066702 (2008), DOI: 10.1103/PhysRevE.77.066702.
- ⁴¹P. Yuan and L. Schaefer, “Equations of state in a lattice Boltzmann model,” *Physics of Fluids* **18**, 042101 (2006), DOI: 10.1063/1.2187070.
- ⁴²Q. Li, K. H. Luo, X. Li, *et al.*, “Forcing scheme in pseudopotential lattice Boltzmann model for multiphase flows,” *Physical Review E* **86**, 016709 (2012), DOI: 10.1103/PhysRevE.86.016709.
- ⁴³Q. Li and K. Luo, “Achieving tunable surface tension in the pseudopotential lattice Boltzmann modeling of multiphase flows,” *Physical Review E* **88**, 053307 (2013), DOI: 10.1103/PhysRevE.88.053307.
- ⁴⁴Q. Li, K. Luo, and X. Li, “Lattice Boltzmann modeling of multiphase flows at large density ratio with an improved pseudopotential model,” *Physical Review E* **87**, 053301 (2013), DOI: 10.1103/PhysRevE.87.053301.
- ⁴⁵D. Lycett-Brown and K. H. Luo, “Improved forcing scheme in pseudopotential lattice Boltzmann methods for multiphase flow at arbitrarily high density ratios,” *Physical Review E* **91**, 023305 (2015), DOI: 10.1103/PhysRevE.91.023305.
- ⁴⁶L. E. Czelusniak, V. P. Mapelli, M. Guzella, L. Cabezas-Gómez, and A. J. Wagner, “Force approach for the pseudopotential lattice Boltzmann method,” *Physical Review E* **102**, 033307 (2020), DOI: 10.1103/PhysRevE.102.033307.
- ⁴⁷R. F. Warming and B. J. Hyett, “The modified equation approach to the stability and accuracy analysis of finite-difference methods,” *Journal of Computational Physics* **14**, 159–179 (1974), DOI: 10.1016/0021-9991(74)90011-4.
- ⁴⁸S. Simonis and M. J. Krause, “Limit consistency of lattice Boltzmann equations,” *ESAIM: M2AN* (2025), DOI: 10.1051/m2an/2025026.
- ⁴⁹H. B. Chae, J. W. Schmidt, and M. R. Moldover, “Surface tension of refrigerants R123 and R134a,” *Journal of Chemical and Engineering Data* **35**, 6–8 (1990), DOI: 10.1021/jc00059a002.
- ⁵⁰C. Oliveira and W. A. Wakeham, “The viscosity of liquid R134a,” *International journal of thermophysics* **14**, 33–44 (1993), DOI: 10.1007/BF00522659.
- ⁵¹C. Oliveira and W. A. Wakeham, “Viscosity of R134a, R32, and R125 at

Saturation,” *International journal of thermophysics* **20**, 365–373 (1999), DOI: 10.1023/A:1022640617694.
⁵²Z. Guo, “Well-balanced lattice Boltzmann model for two-phase systems,”

Physics of Fluids **33** (2021), 10.1063/5.0041446.
⁵³J. S. Rowlinson and B. Widom, *Molecular Theory of Capillarity* (Clarendon Press, Oxford, 1982) p. 327.